This article was published in Applied Catalysis B: Environmental, 147, 988-999, 2014
http://dx.doi.org/10.1016/j.apcatb.2013.09.031

Are TiO_2-based exterior paints useful catalysts for gas-phase photooxidation processes? A case study on *n*-decane abatement for air detoxification

Ricardo A.R. Monteiro[1], Filipe V.S. Lopes[1], Adrián M.T. Silva[2,*], Joana Ângelo[3], Gabriela V. Silva[4], Adélio M. Mendes[3], Rui A.R. Boaventura[1], Vítor J.P. Vilar[1,*]

[1]LSRE - Laboratory of Separation and Reaction Engineering

[2]LCM - Laboratory of Catalysis and Materials

Associate Laboratory LSRE/LCM

Faculdade de Engenharia, Universidade do Porto, Rua Dr. Roberto Frias, 4200-465 Porto, Portugal

[3]LEPAE - Laboratory for Process, Environmental and Energy Engineering

Faculdade de Engenharia, Universidade do Porto, Rua Dr. Roberto Frias, 4200-465 Porto, Portugal

[4]IDMEC - Institute of Mechanical Engineering

Faculdade de Engenharia, Universidade do Porto, Rua Dr. Roberto Frias, 4200-465 Porto, Portugal

[*] Authors to whom correspondence should be addressed:

Tel. +351 918257824; Fax: +351 225081674; E-mail addresses: adrian@fe.up.pt (Adrián M.T. Silva); vilar@fe.up.pt (Vítor J.P. Vilar).

Abstract

n-Decane is a saturated long-chain hydrocarbon, belonging to the family of the volatile organic compounds (VOCs), which is persistently present in indoor air of several industrial closed facilities. Due to the VOCs environmental impact, all efforts that have been made during the last decades to degrade this kind of air pollutants are extremely important. Accordingly, the present paper reports *n*-decane photooxidation studies carried out in an annular photoreactor under simulated solar irradiation and employing a catalytic bed made of cellulose acetate monoliths coated with a photocatalytic paint. The influence of the feed flow rate, *n*-decane concentration, relative humidity, and incident irradiance on the *n*-decane degradation kinetics was assessed. Within this work, *n*-decane photodegradations higher than 90% were achieved, depending on the experimental conditions. Additionally, a phenomenological reaction rate model of the *n*-decane photocatalytic oxidation was proposed and assessed. The proposed model assumes that *n*-decane and water molecules compete for different active sites on the catalyst surface. Finally, despite the high *n*-decane photodegradation achieved, reaction by-products were identified and, based on these compounds, a reaction mechanism was formulated.

Keywords: Photocatalysis; Air Decontamination; *n*-Decane; Photo-TiO_2 Paint; Acetate Cellulose Monoliths; Artificial Sunlight.

1. Introduction

For a long time, society has been debating indoor air pollution and its effect on human health whether in urban or industrial areas [1-4]. Today, 70-90% of our lifetime is spent at indoor environments [5, 6]. Incoming air filters or air cleaners based on ultraviolet germicidal irradiation, activated carbon, ionization, or ozone generation are the most used methods for air decontamination [3, 7]. Nevertheless, photocatalysis is now seen as a valuable option for de-polluting purposes [8-15], mainly because it: i) can be operated at room temperature [16]; ii) air (through water vapour and molecular oxygen) can be used as the source of oxidant [17], iii) degrades/mineralizes a wide range of organic pollutants into harmless or easily neutralized final products (CO_2, H_2O and mineral acids) [18]; iv) can take advantage of solar radiation for performing the charge separation at the semiconductor [19]. Furthermore, semiconductor titanium dioxide (TiO_2) is commonly employed as photocatalyst in photocatalytic oxidation (PCO) processes due to its inexpensiveness, resistance to photocorrosion, high oxidative power, and relatively low toxicity [20-22].

As reported in our previous work [23], high concentrations of *n*-decane (up to 300 $\mu g\ m^{-3}$) were found in the indoor air of a WWTP with closed facilities at different sampling sites and campaigns; thus, *n*-decane was used as organic air pollutant model. The solar PCO of *n*-decane over TiO_2 for air detoxification can be represented by eq. 1 [10]:

$$C_{10}H_{22}(g) + \frac{31}{2}\ O_2(g) \xrightarrow{TiO_2,\ h\upsilon} \text{intermediates} \xrightarrow{TiO_2,\ h\upsilon} 10\ CO_2(g) + 11\ H_2O(g) \qquad \text{(eq. 1)}$$

and considering what is believed to be the initial stages of the photocatalytic process, the following equations are the most representative [24-27]:

$$TiO_2 + h\upsilon \longrightarrow e_{cb}^{-}(TiO_2) + h_{vb}^{+}(TiO_2) \qquad \text{(eq. 2)}$$

$$h_{vb}^{+}(TiO_2) + H_2O \longrightarrow HO^{\bullet} + H^{+} \qquad \text{(eq. 3)}$$

$$h^{+}_{vb}(TiO_2) + HO^{-} \longrightarrow HO^{\bullet} \quad \text{(eq. 4)}$$

$$e^{-}_{cb}(TiO_2) + O_2 \longrightarrow O_2^{\bullet -} \quad \text{(eq. 5)}$$

$$HO^{\bullet} + RH \longrightarrow RH^{\bullet +} \longrightarrow R^{\bullet} + H^{+} \quad \text{(eq. 6)}$$

$$h^{+}_{vb}(TiO_2) + RH \longrightarrow RH^{\bullet +} \longrightarrow R^{\bullet} + H^{+} \quad \text{(eq. 7)}$$

$$O_2^{\bullet -} + H^{+} \longrightarrow HOO^{\bullet} \quad \text{(eq. 8)}$$

$$O_2^{\bullet -} + HOO^{\bullet} + H^{+} \longrightarrow H_2O_2 + O_2 \quad \text{(eq. 9)}$$

Conduction-band electrons $e^{-}_{cb}(TiO_2)$ and valence-band holes $h^{+}_{vb}(TiO_2)$, i.e. electron-hole pairs, are generated when photons of energy $h\upsilon$ matching or exceeding the semiconductor band-gap energy are absorbed (eq. 2). Once at the surface of the semiconductor, and on the absence of any suitable acceptor (for e^{-}_{cb}) and donor (for h^{+}_{vb}) recombination will occur in a matter of nanoseconds; therefore no reaction occurs [16, 27]. Hydroxyl anions and water molecules adsorbed on TiO_2 surface, act as electron donors, while molecular oxygen acts as electron acceptor, leading to the formation of hydroxyl ($HO^{\bullet}$) and superoxide ($O_2^{\bullet -}$) radicals [24-26] (see eq. 3-5). When an organic molecule (RH) is adsorbed onto semiconductor surface, the reaction with hydroxyl radical occur, followed by structural breakdown into several intermediates until, eventually, total mineralization (see eq. 6) [10, 28]. The photogenerated holes due to the high oxidation potential can also participate in the direct oxidation of the organic pollutants (eq. 7) [29, 30]. Peroxide ($HOO^{\bullet}$) radical can also be generated from the protonation of $O_2^{\bullet -}$ radical and subsequently form hydrogen peroxide (see eq. 8-9).

TiO_2 powders have been incorporated as white pigment in different applications from ancient times [31]. As early as 1929, Kiedel [32] stated that titanium white pigment, under sunlight irradiation, was responsible for paint chalking because the photodegradation of organic binder. In 1938, Goodeve *et al.* [33] reported that UV

absorption produces active oxygen species on the TiO_2 surface that cause dyes to photobleach.

Although, it was during the 1960s that, for the first time, TiO_2 photochemical effect was used to induce chemical reactions [34, 35], Mashio and coworkers [36] in 1956 conducted several studies regarding oxidation induced by TiO_2 under illumination. These works concluded that anatase is more photoactive than rutile. However, the first contribution for understanding the heterogeneous photocatalytic effect was in 1972 with the pioneer work by Fujishima and Honda [37]. These authors investigated the electrochemical photolysis of water using a single TiO_2-rutile crystal (n-type) as photoanode and a Pt counter electrode. This work opened the frontiers for the use of titania for photocatalysis and other applications.

Construction materials can be used to support photocatalytic TiO_2 nanoparticles and used as depolluting agents [31, 38-44]. Paint coatings, among all construction materials, are especially attractive as support for photocatalytic TiO_2 since almost all surfaces in urban areas can be painted. Bygott *et al.* [38], for instance, report a field trial in London, close to a school children playground, where an area of 300 m^2 of walls was painted with a silicate-based paint incorporating 7.5 wt.% of photocatalytic TiO_2. The results showed a daily NO_x abatement of ca. 4.5 g in about 10 000 m^3 of air around the school children playground [38]. Maggos *et al.* [44] report NO_x depollution tests in an artificially closed parking area, which was polluted by a car exhaust during the testing period; they observed a reduction of 19 % and 20 % for NO and NO_2, respectively. Salthammer and Fuhrmannh [43] studied the photocatalytic efficiency of two different types of commercially available wall paints in a 1 m^3 test chamber with and without air exchange using artificial daylight. The results showed that formaldehyde was

118 photooxidise under static conditions. In contrast, for typical VOCs, under dynamic
119 conditions, no significant photocatalytic effect was observed.

120 Several studies indicate that paint components can impair the photoactivity of
121 paint films [42-50]. For example, Allen *et al*. [46] studied the effect of different paint
122 components on the photoactivity of these paints. The results showed that the porosity,
123 which is related to the particulated paint components (pigments and extenders)
124 concentration, has a positive effect on photoactivity. However, higher content in $CaCO_3$
125 and high porosity makes paints prone to self-degradation. In the same line, Mendes and
126 co-workers [41, 51, 52] developed a vinyl exterior paint modified with several TiO_2
127 photocatalysts: P25 (Evonik/Degussa), PC50 (Millennium), PC105 (Millennium), PC500
128 (Millennium), ANX type PA (Kemira), UV100 (Sachtleben), AMT100 (Tayca),
129 UVLP7500 (Kronos), VLP7000 (Kronos), and VLP7101 (Kronos); the authors stated that
130 paint pigmentary TiO_2 is the most critical component affecting the photocatalytic activity
131 for NO_x abatement due to its competitive absorption of the UV radiation. Considering the
132 results reported by these authors, the highest yields towards NO_x photocatalytic oxidation
133 are obtained when incorporating in paint formulations photocatalysts PC500
134 (Millennium), PC105 (Millennium), and UV100 (Sachtleben) [41, 51, 52]

135 Although the potential of photocatalytic paints to detoxify air is very promising,
136 several studies demonstrate the formation of by-products that may be harmful for humans
137 [45, 53-55]. For example, Uhde and Salthammer [54] reported that UV-irradiated paints
138 produce undesired and highly toxic by-products such as formaldehyde, acetaldehyde,
139 ethylacrolein, pentanal, 1-hydroxy-butanone, and hexanal. This observation was further
140 emphasized by Kolarik and Toftum [53]. Auvinen *et al.* [45] and Geiss *et al.* [55] found
141 that relatively high amounts of organic compounds, such as aldehydes and ketones, are
142 formed from the decomposition of binders and additives. Auvinen *et al.* [45] also stated

143 that photocatalytic surface aging and the use of different substrates (glass, gypsum or
144 polymeric plaster) do not have a noteworthy influence on the paint photocatalytic activity.
145 Disinfection of air using photocatalytic paints was the focus of other research
146 groups [47, 50, 56]. According to Hochmannova and Vytrasova [47], UV light emitted
147 from normal domestic fluorescent lights is capable to ensure the photocatalytic and
148 antimicrobial effects of paints incorporating nanoparticles of zinc oxide. Later, Sousa *et*
149 *al*. [50] showed microorganism photoinactivation over a photocatalytic paint under UVA
150 irradiation.
151 Although photocatalytic paints have been showing very promising results
152 concerning the photodegradation of air pollutants and the photoinactivation of
153 microorganisms, it is necessary to keep improving their performance paints as well as
154 understand the phenomena behind their photoactivity. This paper presents a study on gas-
155 phase solar photooxidation of *n*-decane over a TiO_2-containing paint, using a lab-scale
156 continuous-flow annular photoreactor with a compound parabolic collector. To the best
157 of our knowledge, this is the first time that the performance of TiO_2-based exterior paints
158 and their applicability on gas-phase photooxidation processes for *n*-decane abatement is
159 evaluated. The photocatalytic oxidation of *n*-decane was studied for different operating
160 conditions, such as feed flow rate, *n*-decane concentration, feed relative humidity and
161 incident irradiance. The *n*-decane degradation reaction behaviour in the continuous
162 system was modelled considering different Langmuir-Hinshelwood kinetic-based
163 reaction rate equations. It considers that PCO of *n*-decane is not influenced by reaction
164 intermediates and/or products and *n*-decane and water are the major species. In addition,
165 a reaction mechanism was proposed for *n*-decane PCO considering the degradation by-
166 products identified by GC/MSD.

2. Experimental

2.1.Materials and chemicals

Mendes and co-workers [41, 51, 52] reported a water-based vinyl paint loaded with TiO_2 photocatalyst PC500 (Millennium) that produced high NO conversions among several other commercially available photocatalysts. For this reason the same modified vinyl paint with photo-TiO_2 PC500 was selected. The PC500 photocatalyst properties are detailed in Table 1. Cellulose acetate monoliths (named C: TIMax CA50-9/S – L_C = 80 mm, d_{ch}^2 = 9 mm × 9 mm, $e_{w,ch}$ = 0.1 mm; Wacotech GmbH & Co. KG.) were used to support the catalytic paint. For the generation of humidified air streams contaminated with *n*-decane, deionized water and *n*-decane (≥ 94%; CAS no. 124-18-5; Merck) were used without further purification. Air Liquide provided all gases, with minimum total purities of 99.999%: helium N50, nitrogen N50, and synthetic air N50 (O_2: 20 ± 1%; H_2O: < 3 ppm; C_nH_m: < 0.1 ppm; CO_2: < 1 ppm; CO: < 1 ppm).

2.2. Photocatalytic films preparation and characterization

Photo-TiO_2 PC500 from Millennium) was used to modify a commercially available exterior water-based vinyl paint. The catalyst and paint properties are summarized in Table 1 [52]. From the original exterior water-based vinyl paint, half of the pigmentary TiO_2 (9 wt.% in wet base) was removed; the photocatalytic paint (henceforth named as P) was, subsequently, formulated by adding 9 wt.% of photo-TiO_2 PC500 (ca. 50 cm^3 of paint without 50% of pigmentary TiO_2 and mixing for 30 min at 300 rpm in a 100 cm^3 stainless steel vessel), as reported by Águia *et al.* [41]. The final photo-TiO_2 PC500 and pigmentary TiO_2 content was 9 wt.% in wet basis (ca. 17 wt.% in dry basis) (see Table 1).

Cellulose acetate monoliths were coated with a thin film of the photocatalytic paint P using the dip-coating method (Dip-Coater RDC21-K, Bungard Elektronik GmbH

192 & Co. KG.) [57]; the photocatalytic paint supported on cellulose acetate monoliths was
193 labelled as PC. Briefly, before coating, cellulose acetate samples were soaked for 1 h with
194 distilled water and alkaline detergent (Derquim LM 01, Panreac Química, S.A.U.),
195 subsequently washed exhaustively with Milli-Q water, and finally, heated up to 323 K to
196 dryness. Then, four layers of photocatalytic paint P were deposited at a withdrawal rate
197 of 0.8 mm s^{-1} until a thin and uniform film was formed on each support surface (these
198 samples were dried at 323 K for 1 h between each layer deposition). Finally, PC samples
199 were packed into an annular photocatalytic reactor (see section 2.4) for the study of
200 *n*-decane degradation through PCO. The catalytic bed properties are also detailed in Table
201 1.

202 Scanning electron microscopy (SEM) coupled with energy dispersive X-ray (EDX)
203 analysis was performed in a FEI Quanta 400 FEG ESEM / EDAX Genesis X4M apparatus
204 equipped with a Schottky field emission gun (for optimal spatial resolution) for the
205 characterization of the surface morphology of PC500 powder, fresh PC, and used PC
206 samples (after more than 50 h of PCO experiments) as well as their chemical composition.
207 Each sample was mounted on a double-sided adhesive tape made of carbon for its surface
208 observation at different magnifications; the cross-section of the fresh PC sample was also
209 measured by this technique. These SEM/EDX analyses were made at CEMUP (Centro de
210 Materiais da Universidade do Porto).

211

212 *2.3. Experimental setup*

213 The experimental setup is depicted in Fig. 1. A full description of the whole
214 apparatus is given elsewhere [58]. The feed generator is composed by three mass flow
215 controllers (MFC, El-Flow, Bronkhorst High-Tech B.V.), which allow the generation of
216 humid air streams contaminated with *n*-decane by flowing air through distinct Woulff

bottles (Normax, Lda.), one containing *n*-decane and another filled with deionized water (Fig. 1a). The photocatalytic system comprises (Fig. 1b): i) a solar simulator (Atlas, model Suntest XLS+) with a working area of 0.110 m^2, a 1.7 kW air-cooled xenon arc lamp, a daylight filter and quartz filter with infrared coating; ii) a compound parabolic collector with 0.023 m^2 of illuminated area with electropolished anodized aluminium reflectors (to use both direct and diffuse irradiation as well to uniform it throughout the bed); iii) photoreactor composed by two concentric and axially centred tubes (the outer tube made of Pyrex-glass, Duran borosilicate glass 3.3, cut-off at 280 nm, Schott-Rorhglas GmbH, and the inner tube made of quartz, Quarzglas-Rohr Quarzglastechnik, GmbH & Co.); iv) an actinic lamp (Actinic BL TL 6 W, Koninklijke Philips Electronics N.V.) for catalyst degassing and activation purposes, placed inside and axially centred in the inner tube (peak at 365 nm – UVA radiation). Both inlet and outlet caps of the photoreactor have four equidistant inlets to ensure a better distribution of the feed stream to the reactor. Note that the tubing for inlets and outlets are made of PTFE (supplied by Vidrolab2, S.A.) that minimizes the adsorption of VOCs. Table 1 also shows the tube dimensions of the photoreactor; Figs. $1b_1$ and $1b_2$ schematically represent the continuous-flow photoreactor from a side and frontal point of view, respectively.

n-Decane concentration histories were monitored using a gas chromatograph (MGC Fast GC, Dani Instruments S.p.A.) equipped with a flame ionisation detector (FID) and a Volcol capillary column (20 m × 0.18 mm × 1.00 μm; Supelco, Sigma-Aldrich Co. LLC.) (see Fig. 1c). The experimental setup was connected to a computer and controlled using a data acquisition board system and an in-house program developed routine written in Labview environment (NI Corporation). All connections are of 1/16" stainless steel tubing (Swagelok Company) to reduce dead volumes.

Additionally, by-products from the *n*-decane photooxidation were analysed at

steady-state, sampling the photoreactor exit stream to a Tedlar bag (232-05SKC, SKC Inc.) and then transferring the sample to stainless steel tubes with Tenax TA60/80 mesh (Supelco, Sigma-Aldrich Co. LLC.). After sampling, identification and quantification of the reaction products was performed with a thermal desorption system (SDT 33.50, Dani Instruments S.p.A.) working in line with a GC/MSD device (a gas chromatograph GC 6890N coupled to a mass spectrometer detector MSD 5973, Agilent Technologies, Inc.). The response factor of toluene (ISO 16000-6 [59]) was used to determine the concentration of the major products (while for *n*-decane, specific response factor were used).

2.4. Photocatalytic experiments

All experiments were carried inside the chamber of the aforementioned solar simulator, which can simulate a spectrum similar to that of sunlight within $300 < \lambda < 800$ nm. The incident irradiance was measured using a broadband UV radiometer (CUV 5, Kipp & Zonen B.V.), placed on the outside of the outer tube and at the same height, within a spectral range of 280 to 400 nm corresponding to the UV fraction of the solar irradiation.

At steady-state, *n*-decane photodegradation fraction ($C_{dec,\,exit} / C_{dec,\,feed}$, where $C_{dec,\,feed}$ and $C_{dec,\,exit}$ in ppm are the pollutant concentration on the feed and exit streams, respectively) was studied for several experimental conditions: feed flow rate (75–300 $cm^3\ min^{-1}$, measured at 1 bar and 298 K), pollutant concentration (40-138 ppm), feed relative humidity (3-40%, measured at 1 bar and 298 K), and incident irradiance (18.9-38.4 $W\ m^{-2}$, measured for the spectral range between 280-400 nm: UV fraction of the incident sunlight). Table 2 summarizes all the experiment conditions. Prior to all experiments, the catalytic bed was degassed and the photocatalytic paint coat activated under UV radiation and by flowing 30 $mL\ min^{-1}$ (measured at 1 bar and 298 K) of synthetic air with 40 % of relative humidity for 24 h (similar conditions as described

elsewhere [41]). Before turning on the solar simulator, the catalytic bed was continuously fed and, by means of outlet stream sampling analysis, the feed composition steadiness was checked.

3. Results and discussion

3.1. Photochemical oxidation of n-*decane*

A blank test consisting in an experiment without photocatalyst was performed, showing no measurable *n*-decane concentration decrease (data not presented; operating conditions reported in Table 2: run 1).

3.2. Photocatalytic oxidation of n-*decane*

3.2.1. Surface characterization of photo-TiO_2 powder and PC samples

The surface morphology of PC500 powder sample and its chemical composition were determined by SEM/EDX. The SEM micrograph (Supplementary Data: Fig. A.1) shows an estimated size of the photo-TiO_2 agglomerates of ca. 600-1500 nm. According to this image, the dimension of the agglomerates range from half size up to the values provided by the manufacturer (see Table 1); similar sizes are displayed in SEM pictures of photocatalytic paint films loaded with the same photocatalyst and reported by Águia *et al.* [51]. As previously mentioned by the same authors [51], EDX analysis of PC500 powder (Supplementary Data: Fig. A.2) indicates that both agglomerates and individual particles are only made of TiO_2.

The surface morphology and chemical composition of PC samples was also determined by SEM/EDX. SEM micrographs of fresh PC and used PC samples (with 50 h+ of use in PCO of *n*-decane) at three different magnifications are shown in Figs. 2a to 2d. The fresh PC images (Figs. 2a and 2c) show that the photocatalytic paint was homogeneously coated on the cellulose acetate monolith. After its use on the PCO experiments (Figs. 2b and 2d), SEM micrographs suggest that the film structure was not

292 significantly affected despite the harsh operating conditions employed. This conclusion
293 was also supported by EDX analysis of both fresh and used samples (shown in Figs. 2e
294 and 2f, respectively). According to the EDX spectra, the proportion of each element
295 remained approximately the same after the photocatalytic experiments. From SEM
296 images (Fig. 3) it was also possible to estimate the paint film thickness (ca. 5-10 μm) and
297 the cellulose acetate monolith thickness (ca. 50 μm). Contrarily to what have been
298 observed by Lopes *et al.* [60] when using TiO_2 sol-gel films supported on cellulose acetate
299 monoliths, paint films are approximately 25-fold thicker (and more resistant) than TiO_2
300 sol-gel films. These properties significantly prevent film fissures, delamination, and/or
301 degradation. Thus, the use of paint films reveals to be an advantage in the prevention of
302 the catalyst/support aging.

303 *3.2.2. Operating parameters effect on n-decane photodegradation*

304 At steady-state conditions, *n*-decane photodegradation fraction ($C_{dec,\ exit}$ / $C_{dec,\ feed}$)
305 was obtained for four experimental conditions (Figs. 4-6). Fig. 4 shows the effect of the
306 feed flow rate (Q_{feed}) on the *n*-decane photodegradation fraction. *n*-decane
307 photodegradation decreases as Q_{feed} increases, since a higher feed flow rate results in a
308 lower residence time, reducing the pollutant-catalyst contact period. Thereby, for a 4-fold
309 increase in Q_{feed}, the photocatalytic process is 1.6, 1.9, and 2.3 times less effective,
310 respectively, for incident irradiances of 38.4, 29.1 and 18.9 W m^{-2} (Table 2: runs 4 and 7,
311 runs 5 and 8, and runs 6 and 9, respectively). This also means that, for a higher feed flow
312 rate the incident irradiance on the catalyst surface becomes more relevant for the PCO of
313 *n*-decane: the electron-hole pairs formation is favoured by higher incident irradiances.

314 In Fig. 5 is shown the influence of the feed concentration on the *n*-decane
315 photodegradation fraction. Results show a decrease in the photodegradation fraction with
316 an increase of *n*-decane concentration. In fact, for a 3.4-fold increase in *n*-decane

317 concentration, 1.8, 2.4, and 3.6 times lower photodegradation fractions were observed for
318 incident irradiances of 38.4, 29.1 and 18.9 W m^{-2}, respectively (Table 2: runs 4 and 7,
319 runs 5 and 8, and runs 6 and 9, respectively). So, increasing the number of *n*-decane
320 molecules that enters the reactor per unit of time, a higher number of photons/hydroxyl
321 radicals are necessary to achieve the same photodegradation. Furthermore, the results
322 above suggest that the feed concentration has a more important influence on the PCO of
323 *n*-decane than the feed flow rate for the same organic load, most likely due to the
324 considerably lower surface area "usefully" available for the photocatalytic reaction. In
325 other words, despite the equivalent UV-irradiated surface area, there are more VOC
326 molecules adsorbed per surface area, restricting the generation of oxidant species from
327 adsorbed water and oxygen (namely, hydroxyl radicals, peroxide radicals, and superoxide
328 radicals).

329 Although there are plenty of studies describing the influence of feed relative
330 humidity on the photodegradation of alkanes, conclusions are still not clear [10, 61].
331 Twesme *et al.* [62] and Zhang and Liu [63] pointed out 40% and 20% of relative humidity,
332 respectively, as the optimum conditions regarding water content to obtain the highest
333 degradation rates in their studies. Shang *et al.* [64] demonstrated in their studies that the
334 degradation rate of *n*-heptane decreases as the relative humidity was increased from 0 to
335 60%. In fact, the presence of vapour water molecules has two opposing effects: i) inhibits
336 the degradation by competitive adsorption to the photocatalyst surface (for feed streams
337 with high water vapour content) [6, 65]; ii) accelerates the degradation by promoting
338 hydroxyl radicals formation [25]. Fig. 6 shows a slight relative increase (3%) of the
339 *n*-decane photodegradation for the highest irradiance value (38.4 W m^{-2}) and within the
340 relative humidity range of 3 % to 40 %. On the other hand, it was found that for the lower
341 irradiance values, particularly for 18.9 W m^{-2}, its effect on the *n*-decane photodegradation

342 becomes more relevant: for the same relative humidity increment, the *n*-decane
343 photodegradation is 3% (from run 16 to run 1) to 25% (from run 18 to run 3) more
344 efficient with a 2-fold reduction of the incident irradiation (from 38.4 to 18.9 W m^{-2}).
345 This supports the important role of hydroxyl radicals in photocatalytic processes due to
346 the lower amount of surface electron-hole pairs available on the catalyst surface to react
347 with the pollutant molecules.

348 It should be pointed out that after 50 h under simulated solar irradiation and
349 continuous feed (humid air contaminated with *n*-decane), similar photodegradations were
350 obtained under the same operating conditions (data not shown). Considering the up-stated
351 for SEM analysis (see section 3.2.1), it is suggested that PC deterioration was negligible.

352 *3.2.3. Simulation and predictive studies of n-decane kinetics through PCO*

353 Several models have been proposed in the literature for simulating VOC
354 photocatalytic oxidation kinetics [58, 60]. Table 3 describes the complete mathematical
355 model combined with three different Langmuir-Hinshelwood reactions rate expressions.
356 The numerical solution of the mathematical model was performed in gPROMS
357 environment (Process System Enterprise, London, UK) using the orthogonal collocation
358 on finite elements method. The number of elements used was 90 with two interior
359 collocation points (third order polynomials) in each element of the photocatalytic bed.
360 The simulations were performed with an absolute and relative tolerance of 1×10^{-5}. First,
361 parameters were estimated using a sequential quadratic programming algorithm [60];
362 then, the mathematical model was employed for simulating the PCO of *n*-decane. Table
363 3 reports the estimated kinetic and adsorption equilibrium parameters.

364 Results shows that the mathematical model with the Langmuir-Hinshelwood
365 kinetic reaction rate expression RE-3 (bimolecular competitive two types of sites rate
366 expression) generally produced better fitting results within the operational conditions

367 studied than models RE-1 or RE-2 (bimolecular competitive one type of sites or
368 bimolecular non-competitive two types of sites rate expressions) (Figs. 4-6). This means
369 that both *n*-decane and water molecules must be considered independent and targeting
370 different active sites of the catalyst surface. The surface active sites competition between
371 the two types of molecules cannot be disregarded because, despite the higher number of
372 parameters required by RE-3, this rate expression is more suitable to describe the
373 experimental data (see the statistical analysis reported in Table 3). Contrarily to the
374 previous reported models of PCO [58, 60], it was necessary to include an incident
375 irradiance exponential order constant (*n*). The radial effect of the UV irradiation passing
376 through the PC samples and its consequent reflection and refraction were not considered;
377 moreover, the mathematical model neglects any partial UV absorption by the PC samples.
378 Nevertheless, the UV irradiance on PCO of *n*-decane could be fitted by an irradiance
379 exponential order constant $n = 0.8$, as can be seen throughout the paper (Figs. 4-6).
380 The closest results to our data regarding gas-phase PCO of *n*-decane were obtained
381 by Debono *et al.* [66]. However, these authors performed UVA-photocatalytic
382 experiments of *n*-decane over TiO_2 powder dispersed at the bottom of a batch reactor, and
383 employing *n*-decane-polluted air stream at ppb level. Therefore and only for these
384 conditions Debono *et al.* [66] were able to provide a photocatalytic lab-scale setup
385 effective for complete *n*-decane photodegradation.
386 Considering that the mathematical model described successfully the reported
387 experiments, simulations can now be performed to obtain insights concerning the effect
388 of each operating variable on the process performance. The effect of the lab-unit
389 geometrical parameters on the PCO of *n*-decane was assessed (*e.g.*, photoreactor length
390 L_R) within the operating condition studied, aiming unit geometric optimization and re-
391 scaling. Fig. 7 shows the *n*-decane photodegradation fraction profiles, considering

392 photoreactors of different lengths (L_R). It can be seen that, when the operating conditions
393 of run 3 are employed (lowest incident irradiance, and intermediate feed flow rate and
394 *n*-decane concentration), a 1.5-fold increase of the photoreactor length yields to a
395 *n*-decane photodegradation enhancement of 85% (see Fig. 7a). Moreover, for a
396 photoreactor 2× longer, complete *n*-decane photodegradation is attained (Fig. 7a). On the
397 other hand, Fig. 7b predicts how *n*-decane photodegradation fraction is affected as a
398 function of the photoreactor length when the highest incident irradiance and feed flow
399 rate are employed (run 7). For a 1.5 times longer photoreactor than the experimentally
400 employed, a 76% *n*-decane photodegradation enhancement is observed. If the reactor is
401 twice the length (L_R = 0.32 m), only 1% of *n*-decane feed is predictively unreacted;
402 complete *n*-decane photodegradation is attained when using a ~3 times longer
403 photoreactor.

404 *3.3. Reaction mechanism for the PCO of n-decane*

405 The degradation mechanisms of alkanes and the corresponding formation of its
406 by-products have been studied recently [61, 64, 66-69]. According to the previously cited
407 authors it was found that ketones and aldehydes are the main intermediates of *n*-decane
408 photochemical reaction. Minabe *et al.* [70] reported that gas-phase photooxidation of long
409 organic chains over TiO_2 thin-films only produces CO_2 and H_2O. It was suggested that
410 both reactants and intermediates were continuously adsorbed on the TiO_2 surface. Within
411 this work, identification and quantification of the *n*-decane photocatalytic reaction by-
412 products were monitored by GC/MSD (Supplementary Data: Table A.1), for the
413 experimental conditions of run 1 (previously described in Table 2). The identified by-
414 products (and their concentration) were: unreacted *n*-decane (4.32 ppm), *n*-hexane (0.035
415 ppm), *n*-heptane (0.028 ppm), *n*-octane (0.007 ppm), *n*-nonane (0.036 ppm), *n*-undecane
416 (0.005 ppm), 4-methylnonane (0.006 ppm), 2,6-dimethyloctane (0.009 ppm), butanoic

417 acid (0.022 ppm), propanoic acid (0.072 ppm), and butanal (0.016 ppm). Therefore and
418 based on the nature of the identified compounds, a reaction mechanism under wet air
419 (40%) is proposed and schematized in scheme 1. According to scheme 1, *n*-decane
420 undergoes a cleavage into radicals – cracking – by a hydroxyl radical. Taking into
421 consideration that alkyl radical stability increases along the series from methyl to primary,
422 followed by secondary, and then by tertiary carbon, the energy required to create them
423 decreases [71]. So, in the case of straight-chain alkanes, secondary carbons are oxidized
424 by hydroxyl radical rather than primary ones. Nonetheless, from scheme 1 and supported
425 by literature [64, 71-73], it is assumed the formation of both primary and secondary alkyl
426 radicals. After homolytic cleavage of *n*-decane four paths can take place: 1) radical
427 recombination generating new alkane hydrocarbons such as *n*-hexane, *n*-octane, or 2,6-
428 dimethyloctane (Table 3); 2) hydrogen abstraction reactions leading to the formation of
429 alkanes and alkenes; 3) reaction with adsorbed O_2 producing a highly reactive superoxide
430 radicals; 4) oxidation by hydroxyl radicals forming alcohols.

431 Several authors [24, 64, 67, 73] reported the rapidly dehydration of alcohols into
432 alkenes or oxidation into corresponding ketones or aldehydes (see scheme 1, path 4);
433 alkenes could be degraded into aldehydes as reported by Djeghri and Teichner [72]
434 whereas aldehydes could suffer double oxidation by hydroxyl radicals into carboxylic
435 acid [24, 74, 75] as it was detected the presence of propanoic and butanoic acid. An
436 alternative approach was suggested by Kominami *et al.* [76] after observing the formation
437 of an ester from the recombination of the aldehyde and its intermediate. Then, according
438 to Augugliaro *et al.* and Peral *et al.* [24, 25], ester could be adsorbed on the TiO_2 surface
439 where it would be dissociated into alkoxy and carboxylate radical. The alkoxy form an
440 aldehyde and the carboxylate radical could produce alkyl radicals and carbon dioxide
441 leading to alkanes after radical recombination or alkenes after hydrogen abstraction

reaction. Carboxylate radical could also be formed by oxidation by hydroxyl radical of carboxylic acid which would lead to the formation of alkyl radicals and CO_2 in a process called decarboxylative dimerization. On the other hand, several authors [77-79] have proposed the reaction between ketones and adsorbed O_2, forming an unstable ketone diolate complex onto the TiO_2 surface. Consequently, the diolate complex would rapidly be dissociated into carboxylate which would lead to the formation of alkyl radicals and carbon dioxide. These radicals would be rapidly oxidized into alcohols and, then, aldehydes [80]. This approach may explain the absence of ketones and presence of butanal.

Considering that $C_{i,\,C\text{-}dec}$ refers to the carbon atoms concentration of compound *i* formed by *n*-decane photodegradation (all unreacted *n*-decane and its by-products produced), it can be defined as:

$$C_{i,C\text{-}dec} = \frac{C_i}{M_i} \cdot n(C) \cdot M(C) \qquad \text{(eq. 8)}$$

where C_i [ppm] and M_i [g mol^{-1}] are the gas phase concentration and molecular weight of compound i, respectively, n(C) is the number of carbon atoms of each component *i* molecule, and M(C) [g mol^{-1}] is the molecular weight of a carbon atom. Thus, the mineralization efficiency (η_{min} in %) can be determined through eq. 9.

$$\eta_{min}[\%] = \left[1 - \frac{\Sigma_i (C_{i,\,C\text{-}dec})_{exit}}{\Sigma_i (C_{i,\,C\text{-}dec})_{feed}}\right] \qquad \text{(eq. 9)}$$

Thus, considering the carbon atoms concentration of each identified and quantified by-product resulting from the *n*-decane molecules photodegradation (experimental conditions reported in Table 1: run 1) more than 99% of the *n*-decane degraded (~94% of *n*-decane fed) was completely mineralized into CO_2 and H_2O. This result is in agreement to what Debono *et al.* [66] disclosed in their previous work: the total carbon atoms concentration of all by-products formed by *n*-decane photodegradation is lower than 5%.

4. Conclusion

The use of an annular lab-photoreactor under simulated solar irradiation has shown to be inefficient for the photochemical reaction of gaseous *n*-decane and extremely effective on the photocatalytic process over a photo-TiO_2 paint. Under simulated solar irradiation, the gas-phase photocatalytic experiments showed that highest *n*-decane photodegradation (98%) was attained at the lowest Q_{feed} (75 $cm^3\ min^{-1}$) and $C_{dec,\ feed}$ (41 ppm), and highest RH_{feed} (40%) and I (38.4 W m^{-2}). Feeding the photoreactor with the double flow rate, the *n*-decane photodegradation decreases from 96 to 62% (run 1 and 7). Alternatively, when the *n*-decane concentration on the feed stream is doubled, the remaining unreacted *n*-decane fed drops from 4 to 46% (run 1 and 13). It was also observed that the water vapour content effect on the PCO of *n*-decane is more pronounced under lower irradiances, i.e., from ~71 to 56% (run 3 and 18).

A phenomenological model, assuming a Langmuir-Hinshelwood mechanism (bimolecular competitive with two types of sites) was able to describe the *n*-decane photodegradation. It was observed proposed that both species compete for adsorption within different specific active sites (type 1 and 2) of the catalyst surface. Considering the type of by-products identified, a reaction mechanism for *n*-decane photodegradation under the conditions used was proposed.

For all reasons stated before and considering the well-known wide range of paint applications, the results reported seem quite promising for the treatment of indoor and outdoor air. Further research should focus in studying the role of interfering pollutants, as NO_2, and also the eventual production of acetaldehyde and formaldehyde as sub-products.

Acknowledgements

Financial support for this work was mainly provided by the FCT (Fundação para a Ciência e a Tecnologia) project PTDC/EQU-EQU/100554/2008. This work was also supported by project PEst-C/EQB/LA0020/2011, financed by FEDER through COMPETE – Programa Operacional Factores de Competitividade and by FCT. V.J.P. Vilar acknowledges financial support from Programme Ciência 2008 (FCT). R.A.R. Monteiro and J. Ângelo gratefully acknowledge FCT for their PhD Research Fellowships, SFRH/BD/69323/2010 and SFRH/BD/79974/2011, respectively. F.V.S. Lopes also gratefully acknowledge FCT for his Post-doc Research Fellowship, SFRH/BPD/73894/2010.

Appendix A. Supplementary Data

References

[1] C.H. Ao, S.C. Lee, C.L. Mak, L.Y. Chan, Appl. Catal. B: Environ. 42 (2003) 119.

[2] A.T. Hodgson, H. Destaillats, D.P. Sullivan, W.J. Fisk, Indoor Air 17 (2007) 305.

[3] J. Mo, Y. Zhang, Q. Xu, J.J. Lamson, R. Zhao, Atmos. Environ. 43 (2009) 2229.

[4] S.A. Grinshpun, A. Adhikari, T. Honda, K.Y. Kim, M. Toivola, K.S. Ramchander Rao, T. Reponen, Environ. Sci. Technol. 41 (2006) 606.

[5] M.A. Isbell, R.J. Stolzberg, L.K. Duffy, Sci. Total Environ. 345 (2005) 31.

[6] S. Wang, H.M. Ang, M.O. Tade, Environment International 33 (2007) 694.

[7] J. Zhao, X. Yang, Build. Environ. 38 (2003) 645.

[8] C. Srinivasan, N. Somasundaram, Curr. Sci. 85 (2003) 1431.

[9] D.Y. Goswami, J. Sol. Energy Eng. 119 (1997) 107.

[10] M.R. Hoffmann, S.T. Martin, W. Choi, D.W. Bahnemann, Chem. Rev. 95 (1995) 69.

[11] D.S. Bhatkhande, V.G. Pangarkar, A.A.C.M. Beenackers, J. Chem. Technol. Biot. 77 (2002) 102.

[12] C. McCullagh, J. Robertson, D. Bahnemann, P. Robertson, Res. Chem. Intermediat. 33 (2007) 359.

[13] D. Bahnemann, Sol. Energy 77 (2004) 445.

[14] R.W. Matthews, J. Chem. Soc., Faraday Trans. 1 80 (1984) 457.

[15] J.M. Herrmann, Top. Catal. 34 (2005) 49.

[16] A.L. Linsebigler, G. Lu, J. Yates, J. T., Chem. Rev. 95 (1995) 735.

[17] M. Hernandez-Alonso, I. Tejedor-Tejedor, J. Coronado, J. Soria, M. Anderson, Thin Solid Films 502 (2006) 125.

[18] C. Guillard, J. Disdier, C. Monnet, J. Dussaud, S. Malato, J. Blanco, M.I. Maldonado, J.-M. Herrmann, Appl. Catal. B: Environ. 46 (2003) 319.

528 [19] M.L. Satuf, R.J. Brandi, A.E. Cassano, O.M. Alfano, Appl. Catal. B: Environ. 82
529 (2008) 37.
530 [20] E.M. Rossi, L. Pylkkänen, A.J. Koivisto, M. Vippola, K.A. Jensen, M. Miettinen,
531 K. Sirola, H. Nykäsenoja, P. Karisola, T. Stjernvall, E. Vanhala, M. Kiilunen, P. Pasanen,
532 M. Mäkinen, K. Hämeri, J. Joutsensaari, T. Tuomi, J. Jokiniemi, H. Wolff, K. Savolainen,
533 S. Matikainen, H. Alenius, Toxicol. Sci. 113 (2010) 422.
534 [21] C.M. Sayes, R. Wahi, P.A. Kurian, Y. Liu, J.L. West, K.D. Ausman, D.B.
535 Warheit, V.L. Colvin, Toxicol. Sci. 92 (2006) 174.
536 [22] R. Zhang, Y. Bai, B. Zhang, L. Chen, B. Yan, J. Hazard. Mater. 211–212 (2012)
537 404.
538 [23] J.V. Teixeira, S.M. Miranda, R.A.R. Monteiro, F.V.S. Lopes, J. Madureira, G.V.
539 Silva, N. Pestana, E. Pinto, V.J.P. Vilar, R.A.R. Boaventura, Environ. Monit. Assess. 185
540 (2013) 59.
541 [24] J. Peral, D.F. Ollis, J. Catal. 136 (1992) 554.
542 [25] V. Augugliaro, S. Coluccia, V. Loddo, L. Marchese, G. Martra, L. Palmisano, M.
543 Schiavello, Appl. Catal. B: Environ. 20 (1999) 15.
544 [26] E. Pelizzetti, C. Minero, Electrochim. Acta 38 (1993) 47.
545 [27] A. Furube, T. Asahi, H. Masuhara, H. Yamashita, M. Anpo, Chem. Phys. Lett.
546 336 (2001) 424.
547 [28] Y.V. Kolen'ko, K.A. Kovnir, A.I. Gavrilov, A.V. Garshev, P.E. Meskin, B.R.
548 Churagulov, M. Bouchard, C. Colbeau-Justin, O.I. Lebedev, G. Van Tendeloo, M.
549 Yoshimura, J. Phys. Chem. B 109 (2005) 20303.
550 [29] F. Benoit-Marquié, U. Wilkenhöner, V. Simon, A.M. Braun, E. Oliveros, M.-T.
551 Maurette, J. Photoch. Photobio. A 132 (2000) 225.
552 [30] L. Cermenati, P. Pichat, C. Guillard, A. Albini, J. Phys. Chem. B 101 (1997) 2650.

553 [31] A. Fujishima, K. Hashimoto, T. Watanabe, TiO_2 Photocatalysis: Fundamentals
554 and Applications, Bkc, Incorporated, 1999.
555 [32] E. Keidel, Furben Zeitung 34 (1929) 1242.
556 [33] C.F. Goodeve, J.A. Kitchener, T. Faraday Soc. 34 (1938) 570.
557 [34] H. Gerischer, in: H. Eyring, D. Henderson, W. Jost (Eds.), Physical Chemistry,
558 An Advanced Treatise, Academic Press, New York, 1970, pp. 463.
559 [35] V.A. Myamlin, Y.V. Pleskov, Electrochemistry of Semiconductors, Plenum
560 Press, 1967.
561 [36] S. Kato, F. Mashio, Abtr. Book Annu. Meet. Chem. Soc. Jpn. (1956) 223.
562 [37] A. Fujishima, K. Honda, Nature 238 (1972) 37.
563 [38] C.E. Bygott, J.E. Maltby, J.L. Stratton, R. McIntyre, Photocatalytic coatings for
564 the construction industry International RILEM Symposium on Photocatalysis,
565 Environment and Construction Materials, 8–9 October, Florence, Italy, 2007, pp. 251.
566 [39] O. d'Hennezel, P. Pichat, D.F. Ollis, J. Photoch. Photobio. A 118 (1998) 197.
567 [40] A. Bouzaza, A. Laplanche, J. Photoch. Photobio. A 150 (2002) 207.
568 [41] C. Águia, J. Ângelo, L.M. Madeira, A. Mendes, Catal. Today 151 (2010) 77.
569 [42] J. Chen, C.-s. Poon, Build. Environ. 44 (2009) 1899.
570 [43] T. Salthammer, F. Fuhrmann, Environ. Sci. Technol. 41 (2007) 6573.
571 [44] T. Maggos, J.G. Bartzis, M. Liakou, C. Gobin, J. Hazard. Mater. 146 (2007) 668.
572 [45] J. Auvinen, L. Wirtanen, Atmos. Environ. 42 (2008) 4101.
573 [46] N.S. Allen, M. Edge, G. Sandoval, J. Verran, J. Stratton, J. Maltby, Photochem.
574 Photobiol. 81 (2005) 279.
575 [47] L. Hochmannova, J. Vytrasova, Prog. Org. Coat. 67 (2010) 1.
576 [48] S. Laufs, G. Burgeth, W. Duttlinger, R. Kurtenbach, M. Maban, C. Thomas, P.
577 Wiesen, J. Kleffmann, Atmos. Environ. 44 (2010) 2341.

578 [49] A. Costa, G.L. Chiarello, E. Selli, M. Guarino, J. Environ. Manage. 96 (2012) 86.
579 [50] V.M. Sousa, C.M. Manaia, A. Mendes, O.C. Nunes, J. Photoch. Photobio. A 251
580 (2013) 148.
581 [51] C. Aguia, J. Angelo, L.M. Madeira, A. Mendes, J. Environ. Manage. 92 (2011)
582 1724.
583 [52] C. Águia, J. Ângelo, L.M. Madeira, A. Mendes, Polym. Degrad. Stabil. 96 (2011)
584 898.
585 [53] J. Kolarik, J. Toftum, Build. Environ. 57 (2012) 396.
586 [54] E. Uhde, T. Salthammer, Atmos. Environ. 41 (2007) 3111.
587 [55] O. Geiss, C. Cacho, J. Barrero-Moreno, D. Kotzias, Build. Environ. 48 (2012)
588 107.
589 [56] C. Chawengkijwanich, Y. Hayata, Int. J. Food Microbiol. 123 (2008) 288.
590 [57] M.A. Anderson, L.W. Miller, M.I. Tejedor-Anderson, Waveguide, United States
591 Patent, Wisconsin Alumni Research Foundation (Madison, WI, US), 2001.
592 [58] F.V.S. Lopes, R.A.R. Monteiro, A.M.T. Silva, G.V. Silva, J.L. Faria, A.M.
593 Mendes, V.J.P. Vilar, R.A.R. Boaventura, Chem. Eng. J. 204–206 (2012) 244.
594 [59] ISO 16000-6. Determination of volatile organic compounds in indoor and test
595 chamber air by active sampling on Tenax TA sorbent, thermal desorption and gas
596 chromatography using MS or MS/FID, 2004.
597 [60] F.V.S. Lopes, S.M. Miranda, R.A.R. Monteiro, S.D.S. Martins, A.M.T. Silva, J.L.
598 Faria, R.A.R. Boaventura, V.J.P. Vilar, Appl. Catal. B: Environ. 140-141 (2013) 444.
599 [61] A.K. Boulamanti, C.J. Philippopoulos, Atmos. Environ. 43 (2009) 3168.
600 [62] T.M. Twesme, D.T. Tompkins, M.A. Anderson, T.W. Root, Appl. Catal. B:
601 Environ. 64 (2006) 153.
602 [63] P. Zhang, J. Liu, J. Photoch. Photobio. A 167 (2004) 87.

603 [64] J. Shang, Y. Du, Z. Xu, Chemosphere 46 (2002) 93.
604 [65] S. Yamazaki, H. Tsukamoto, K. Araki, T. Tanimura, I. Tejedor-Tejedor, M.A.
605 Anderson, Appl. Catal. B: Environ. 33 (2001) 109.
606 [66] O. Debono, F. Thévenet, P. Gravejat, V. Héquet, C. Raillard, L. Le Coq, N.
607 Locoge, J. Photoch. Photobio. A 258 (2013) 17.
608 [67] N. Djeghri, M. Formenti, F. Juillet, S.J. Teichner, Faraday Discuss. Chem. Soc.
609 58 (1974) 185.
610 [68] R. Nakamura, S. Sato, J. Phys. Chem. B 106 (2002) 5893.
611 [69] W. Balcerski, S.Y. Ryu, M.R. Hoffmann, Int. J. Photoenergy 2008 (2008) Article
612 ID 964721. DOI:10.1155/2008/964721.
613 [70] T. Minabe, D.A. Tryk, P. Sawunyama, Y. Kikuchi, K. Hashimoto, A. Fujishima,
614 J. Photoch. Photobio. A 137 (2000) 53.
615 [71] K.P.C. Vollhardt, N.E. Schore, Organic chemistry: structure and function, 3rd
616 Edition ed., W. H. Freeman and company, New York, 1999.
617 [72] N. Djeghri, S.J. Teichner, J. Catal. 62 (1980) 99.
618 [73] C. Hägglund, B. Kasemo, L. Österlund, J. Phys. Chem. B 109 (2005) 10886.
619 [74] E. Obuchi, T. Sakamoto, K. Nakano, F. Shiraishi, Chem. Eng. Sci. 54 (1999)
620 1525.
621 [75] X. Ye, D. Chen, J. Gossage, K. Li, J. Photoch. Photobio. A 183 (2006) 35.
622 [76] H. Kominami, H. Sugahara, K. Hashimoto, Catal. Commun. 11 (2010) 426.
623 [77] C. Raillard, V. Héquet, P. Le Cloirec, J. Legrand, Water Sci. Technol. 53 (2006)
624 107.
625 [78] M.A. Henderson, Surf. Sci. 602 (2008) 3188.
626 [79] M.A. Henderson, J. Catal. 256 (2008) 287.
627 [80] E. Piera, J.A. Ayllón, X. Doménech, J. Peral, Catal. Today 76 (2002) 259.

628 [81] T. Valdés-Solís, M.J.G. Linders, F. Kapteijn, G. Marbán, A.B. Fuertes, Chem.
629 Eng. Sci. 59 (2004) 2791.
630 [82] G.I. Taylor, P. Roy. Soc. Lond. A. Mat. 219 (1953) 186.
631 [83] A. Aris, P. Roy. Soc. Lond. A. Mat. 235 (1956) 67.
632 [84] D.M. Ruthven, Principal of adsorption and adsorption processes, John Wiley &
633 Sons, New York, 1984.
634 [85] B.E. Poling, J.M. Prausnitz, J.P. O'Connell, The properties of gases and liquids,
635 5th Edition ed., McGraw-Hill, New York, 2001.
636 [86] E.N. Fuller, K. Ensley, J.C. Giddings, J. Phys. Chem. 73 (1969) 3679.
637 [87] E.N. Fuller, J.C. Giddings, J. Chromatogr. Sci. 3 (1965) 222.
638 [88] E.N. Fuller, P.D. Schettler, J.C. Giddings, Ind. Eng. Chem. 58 (1966) 18.
639 [89] C.N. Satterfield, Mass transfer in heterogeneous catalysis, MIT Press,
640 Massachusetts Institute of Technology, Cambridge, MA, USA, 1970.
641 [90] G. Li Puma, I. Salvadó-Estivill, T.N. Obee, S.O. Hay, Sep. Purif. Technol. 67
642 (2009) 226.
643 [91] K.-H. Wang, H.-H. Tsai, Y.-H. Hsieh, Appl. Catal. B: Environ. 17 (1998) 313.
644 [92] T.N. Obee, R.T. Brown, Environ. Sci. Technol. 29 (1995) 1223.
645 [93] T.N. Obee, Environ. Sci. Technol. 30 (1996) 3578.
646 [94] T.N. Obee, S.O. Hay, Environ. Sci. Technol. 31 (1997) 2034.
647 [95] J. Peral, X. Domènech, D.F. Ollis, J. Chem. Technol. Biot. 70 (1997) 117.

648

649

Table captions

Table 1. Catalyst and paint properties; catalytic bed characteristics; photoreactor dimensions employed in the gas-phase PCO of *n*-decane under simulated solar irradiation.

Table 2. Experimental conditions employed in the study of *n*-decane photodegradation.

Table 3. Mathematical model, boundary conditions, kinetic reaction rate expressions used for estimation of the kinetic and adsorption equilibrium parameters of the PCO of *n*-decane; Estimated kinetic and adsorption equilibrium parameters of the mathematical model.

Figure Captions

Fig. 1. Schematic representation of the experimental set-up and the continuous-flow photoreactor: a) lab-scale unit used for the generation of air streams containing *n*-decane and water vapour; b) sunlight simulator containing the photoreactor: b_1) from a side point of view and b_2) from a frontal point of view; c) master gas chromatograph analytic system used for the analysis of the photoreactor feed and exit streams. Reprinted (adapted) with permission from Lopes *et al.* [58]. Copyright © 2012, Elsevier.

Fig. 2. SEM micrographs (a-d) and EDX spectra (e, f) of PC before (left-side images) and after 50 h+ of use (right-side images) in PCO of *n*-decane.

Fig. 3. Photographs (a-b) and SEM micrographs (c-d) of PC after 50 h+ of use in PCO of *n*-decane.

Fig. 4. Influence of feed flow rate (Q_{feed}) on *n*-decane photodegradation fraction ($C_{dec,\,exit}$ / $C_{dec,\,feed}$, at steady-state conditions): experimental points for incident irradiances measured within 280-400 nm (sunlight UV fraction) of 38.4 $W \cdot m^{-2}$ (◆), 29.1 $W \cdot m^{-2}$ (■), and 18.9 $W \cdot m^{-2}$ (▲), and RE-1 (- - -), RE-2 (— · —), and RE-3 (——); $C_{dec,\,feed}$ = 73 ppm, $RH_{feed}{}^{a}$ = 40%, and T = 298 K; operation conditions reported in Table 1; * measured at 298 K and 1 bar.

Fig. 5. Influence of the inlet concentration ($C_{dec,\,feed}$) on *n*-decane photodegradation fraction ($C_{dec,\,exit}$ / $C_{dec,\,feed}$, at steady-state conditions): experimental points for incident irradiances measured within 280-400 nm (sunlight UV fraction) of 38.4 $W \cdot m^{-2}$ (◆), 29.1 $W \cdot m^{-2}$ (■), and 18.9 $W \cdot m^{-2}$ (▲), and RE-1 (- - -), RE-2 (— · —), and RE-3 (——); $Q_{feed}{}^{*}$ = 150 $cm^3 \cdot min^{-1}$, $RH_{feed}{}^{a}$ = 40%, and T = 298 K; operation conditions reported in Table 2; * measured at 298 K and 1 bar.

Fig. 6. Influence of the feed relative humidity (RH_{feed}) on *n*-decane photodegradation fraction ($C_{dec,\,exit}$ / $C_{dec,\,feed}$, at steady-state conditions): experimental points for incident

irradiances measured within 280-400 nm (sunlight UV fraction) of 38.4 (◆), 29.1 (■), and 18.9 W·m^{-2} (▲), and RE-1 (- - -), RE-2 (— · —), and RE-3 (——); Q_{feed}^{*} = 150 cm^3·min^{-1}, $C_{dec,\ feed}$ = 73 ppm, and T = 298 K; operation conditions reported in Table 2; * measured at 298 K and 1 bar.

Fig. 7. *n*-Decane photodegradation fraction profiles ($C_{dec,\ exit}/C_{dec,\ feed}$, at steady-state conditions) for photoreactors with different lengths [L_R]: 0.16 (—), 0.24 (– – –), 0.32 (- - -), and 0.48 m (· · ·); (a) $C_{dec,\ feed}$ = 73 ppm, Q_{feed}^{*} = 150 mL min^{-1}, and I = 18.9 W m^{-2} (measured within 280-400 nm: sunlight UV fraction); (b) $C_{dec,\ feed}$ = 73 ppm, Q_{feed}^{*} = 300 mL min^{-1}, and I = 38.4 W m^{-2} (measured within 280–400 nm: sunlight UV fraction); RH_{feed}^{*} = 30%, and T = 298 K; operation conditions reported in Table 2 (runs 3 and 7, respectively) (* measured at 298 K and 1 bar); experimental data (points); mathematical modelling with RE-3 (lines).

Scheme Captions

Scheme 1. Schematic representation of the reaction pathways proposed for the gas-phase degradation of *n*-decane under simulated solar irradiation (R: alkyl roots or hydrogen).

Table 1
Catalyst and paint properties; catalytic bed characteristics; photoreactor dimensions employed in the gas-phase PCO of *n*-decane under simulated solar irradiation.

Catalyst and Paint [51, 52]		
PC500	Manufacturer	PC500 (Millennium)
	Crystal structure	>99% Anatase
	Crystal size [nm]	5-10
	Shape	Agglomerates
	Surface area [m^2 g^{-1}]	345
	Agglomerate size [μm]	1.2-1.7
	Shape	Agglomerates
Exterior water-based vinyl paint	Pigmentary TiO_2	18 wt.% (wet basis)
	Water	30 wt.% (wet basis)
	Extenders ($CaCO_3$ and silicates)	18 wt.% (wet basis)
	Polymer extender slurry	8 wt.% (wet basis)
	Binder slurry	20 wt.% (wet basis)
	Additives (in slurry)	6 wt.% (wet basis)
Catalytic bed (PC)		
Catalyst (P)	*TiO_2 content (wet basis)*	
	Pigmentary	9 wt.% (wet basis)
	PC500	9 wt.% (wet basis)
	Thin-film properties	
	m_P [g]	1.052
	ρ_P [g cm^{-3}]	2.61
Support (C)	m_C [g]	2.006
	ρ_C [g cm^{-3}]	1.30
	d_{ch} [cm]	0.9
Porosity	ε	0.991
Photoreactor		
Outer tube (Pyrex-glass)	$d_{ot,e}$ [cm]	5.00
	$d_{ot,i}$ [cm]	4.64
Inner tube (quartz)	$d_{in,e}$ [cm]	2.00
	$d_{in,i}$ [cm]	1.64
Photoreactor	L_R [cm]	16.0
	V_R [cm^3]	220

699

Table 2
Experimental conditions employed in the study of *n*-decane photodegradation.

Run	Q_{feed} * [$cm^3\ min^{-1}$]	$C_{dec,\ feed}$ [ppm]	RH_{feed} * [%]	I # [$W\ m^{-2}$]
1 a)	150	73	40	38.4
2	150	73	40	29.1
3	150	73	40	18.9
4	75	73	40	38.4
5	75	73	40	29.1
6	75	73	40	18.9
7	300	73	40	38.4
8	300	73	40	29.1
9	300	73	40	18.9
10	150	40	40	38.4
11	150	40	40	29.1
12	150	40	40	18.9
13	150	138	40	38.4
14	150	138	40	29.1
15	150	138	40	18.9
16	150	73	3	38.4
17	150	73	3	29.1
18	150	73	3	18.9

* Measured at 298 K and 1 bar.
# Measured within 280–400 nm (sunlight UV fraction).
a) Operating conditions used for photochemical experiment.

700

Table 3
Mathematical model, boundary conditions, kinetic reaction rate expressions used for estimation of the kinetic and adsorption equilibrium parameters of the PCO of *n*-decane; Estimated kinetic and adsorption equilibrium parameters resulting of the mathematical model.

Mathematical model, correlations, parameters, and boundary conditions [58, 60]				
Material balance for each component *i*	$\frac{d}{dz}\left(\varepsilon D_{ax}\frac{dC_i}{dz}\right)-\frac{d}{dz}\left(\bar{u}_{0,ch}C_i\right)-\nu_i r=0$			
Axial dispersion (laminar flow) [81-84]	$D_{ax}=D_m+(1/192)\left[\left(\bar{u}_{0,ch}^2 d_{ch}^2\right)/\left(\varepsilon D_m\right)\right]$			
Molecular diffusivity of the mixture	$D_m\cong\frac{1}{N}\sum_{i=1}^{N}D_{m,i}$, with $D_{m,i}=(1-y_i)\sum_{\substack{i=1\\ j\neq i}}^{n}\frac{D_{ij}}{y_i}$			
Binary diffusion coefficient [85-88]	$D_{ij}=\frac{1.41\times10^{-7}T^{1.75}\left[½\left(M_i^{-1}+M_j^{-1}\right)\right]^{1/2}}{p\left[\left(\Sigma_v\right)_i^{1/3}+\left(\Sigma_v\right)_j^{1/3}\right]^2}$			
Superficial velocity (in the cross-section of each channel)	$\bar{u}_{0,ch}=Q_{feed}\left[\pi\left(½d_{ot,i}\right)^2-\pi\left(½d_{in,e}\right)^2\right]^{-1}$			
Component i	N_2	O_2	H_2O	dec
M_i [g·mol^{-1}]	28.01	32.00	18.02	142.28
$(\Sigma_v)_i$	18.5	16.3	13.1	209.8
Boundary conditions	Photoreactor feed ($z=0$): $u_{0,feed}C_{i,feed}=\bar{u}_{0,ch}C_i-\varepsilon D_{ax}\left.\frac{dC_i}{dz}\right\|_{z=0}$		Photoreactor exit ($z=L_R$): $\left.\frac{dC_i}{dz}\right\|_{z=L_R}=0$	
Kinetic reaction rate expressions [3, 6, 58, 60, 89-95]				
RE-1	$r_{dec}=I^n\cdot k\left(\frac{K_{dec}K_{H_2O}C_{dec}C_{H_2O}}{\left(1+K_{dec}K_{H_2O}C_{dec}C_{H_2O}\right)^2}\right)$ *Langmuir-Hinshelwood bimolecular competitive one type of sites*			
RE-2	$r_{dec}=I^n\cdot k\left(\frac{K_{dec}C_{dec}}{1+K_{dec}C_{dec}}\right)\left(\frac{K_{H_2O}C_{H_2O}}{1+K_{H_2O}C_{H_2O}}\right)$ *Langmuir-Hinshelwood bimolecular non-competitive two types of sites*			
RE-3	$r_{dec}=I^n\cdot k\left(\frac{K_{dec}C_{dec}}{1+K_{dec}C_{dec}+K_{H_2O}C_{H_2O}}\right)\left(\frac{K'_{H_2O}C_{H_2O}}{1+K'_{dec}C_{dec}+K'_{H_2O}C_{H_2O}}\right)$ *Langmuir-Hinshelwood bimolecular competitive two types of sites*			
Estimated parameters				
Kinetic reaction rate expressions		RE-1	RE-2	RE-3
Kinetic and adsorption equilibrium parameters	n	0.8	0.8	0.8
	k [mol m^{-2} s^{-1} (W^{-1} m^2)^n]	1.0×10^{-5}	3.2×10^{-6}	2.8×10^{-6}
	K_{dec} [M^{-1}]	13	2205	4498
	K_{H_2O} [M^{-1}]	9.7×10^{-5}	1.5×10^{-4}	1.0×10^{-8}
	K'_{dec} [M^{-1}]	—	—	905
	K'_{H_2O} [M^{-1}]	—	—	4.6×10^{-4}
Statistics	R^2	0.764	0.912	0.954
	$S^2_R\times10^7$ [mol^2 m^{-4} s^{-2}]	3.84	1.43	0.874

701

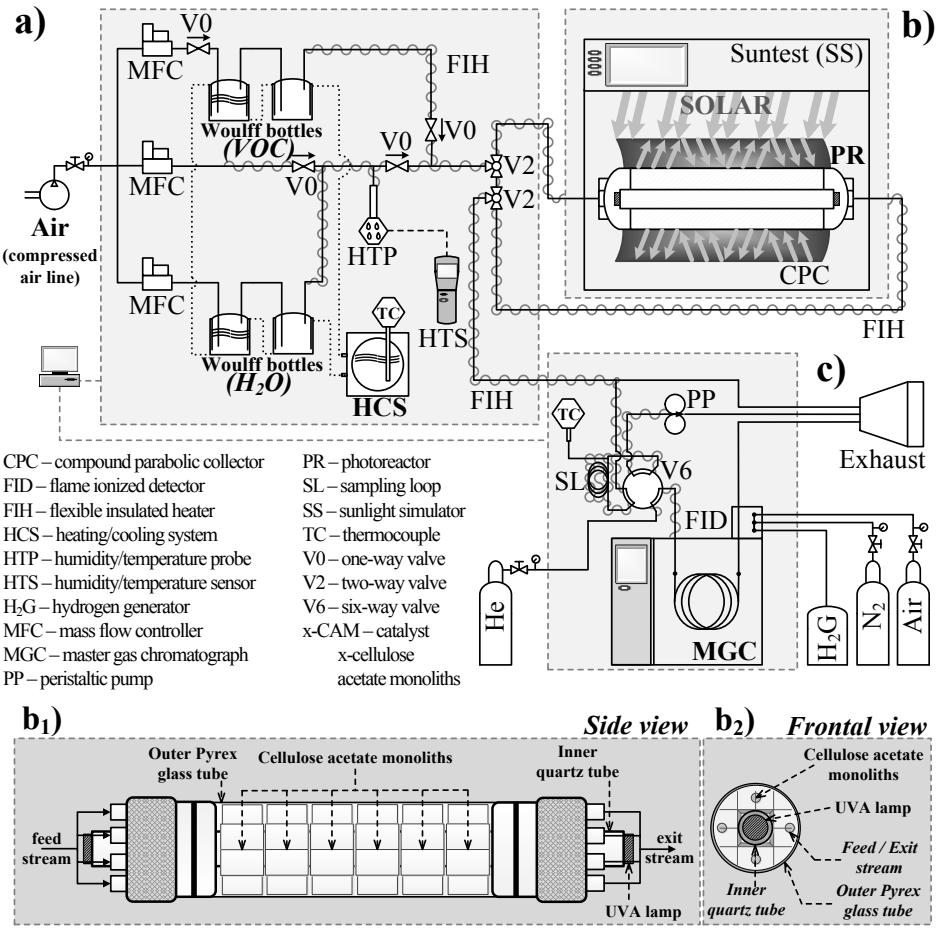

Fig. 1. Schematic representation of the experimental set-up and the continuous-flow photoreactor: a) lab-scale unit used for the generation of air streams containing *n*-decane and water vapour; b) sunlight simulator containing the photoreactor: b_1) from a side point of view and b_2) from a frontal point of view; c) master gas chromatograph analytic system used for the analysis of the photoreactor feed and exit streams. Reprinted (adapted) with permission from Lopes *et al.* [58]. Copyright © 2012, Elsevier.

711

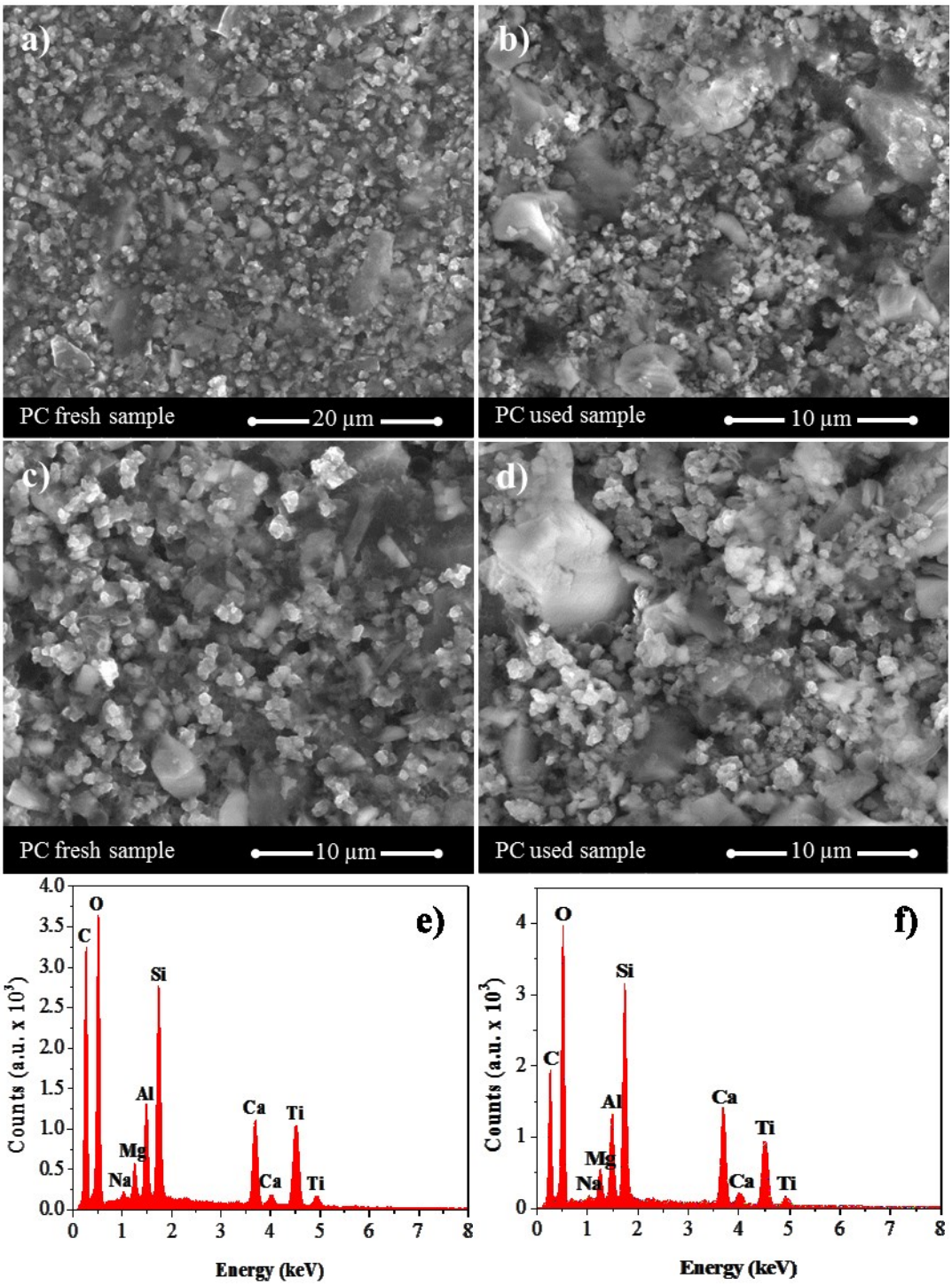

712

713 **Fig. 2.** SEM micrographs (a-d) and EDX spectra (e, f) of PC before (left-side images) and

714 after 50 h+ of use (right-side images) in PCO of *n*-decane.

715

716

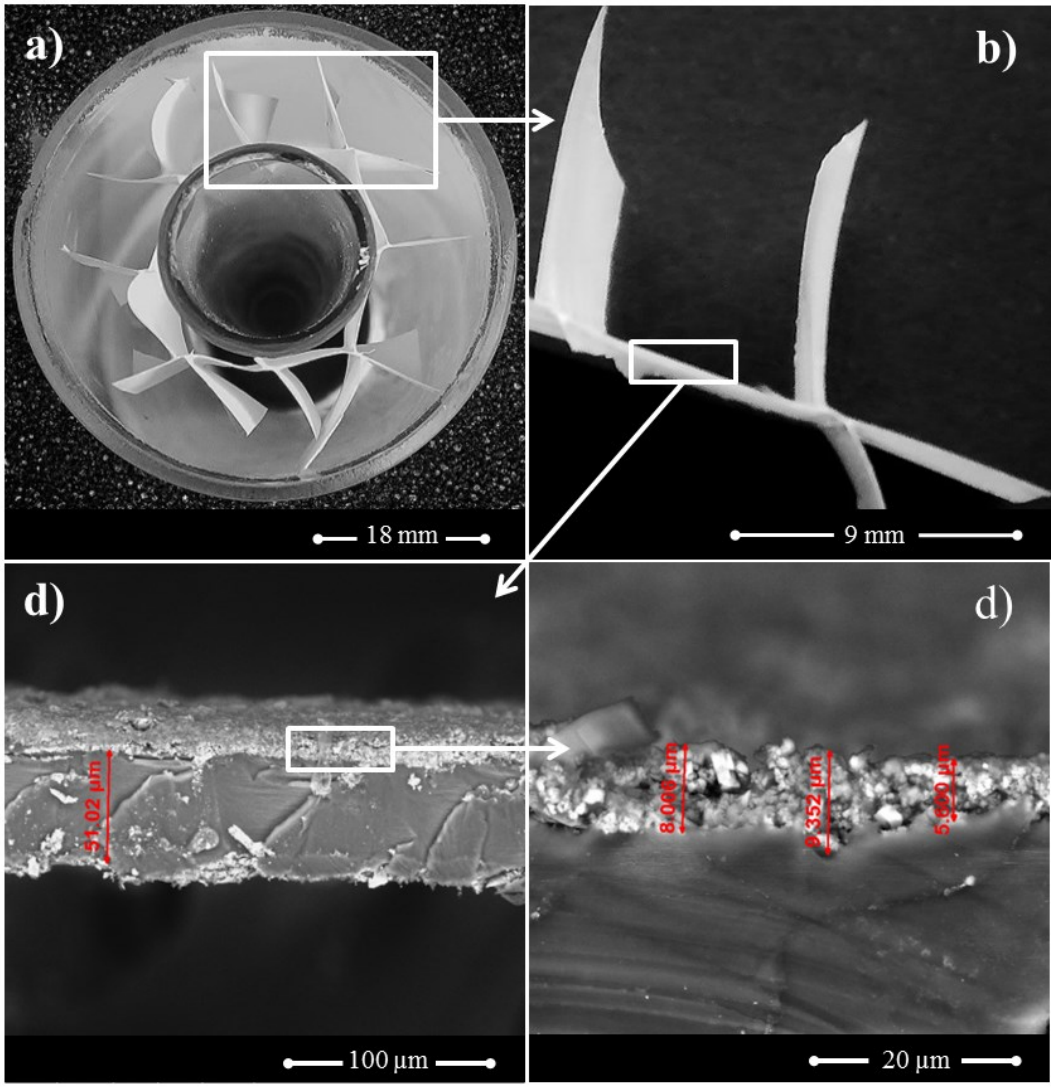

717

718 **Fig. 3.** Photographs (a-b) and SEM micrographs (c-d) of PC used in PCO of *n*-decane.

719

720

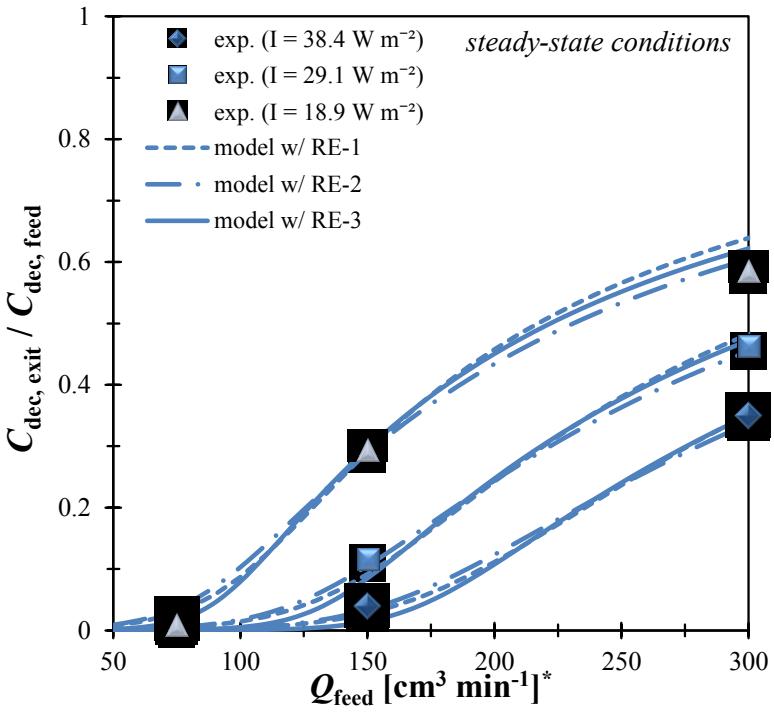

721

722 **Fig. 4.** Influence of feed flow rate (Q_{feed}) on *n*-decane photodegradation fraction
723 ($C_{dec, exit}$ / $C_{dec, feed}$, at steady-state conditions): experimental points for incident irradiance
724 measured within 280-400 nm (sunlight UV fraction) of 38.4 W·m^{-2} (◆), 29.1 W·m^{-2} (■),
725 and 18.9 W·m^{-2} (▲), and RE-1 (- - -), RE-2 (— · —), and RE-3 (——); $C_{dec, feed}$ = 73 ppm,
726 RH_{feed}^{a} = 40%, and T = 298 K; operation conditions reported in Table 1; * measured at
727 298 K and 1 bar.

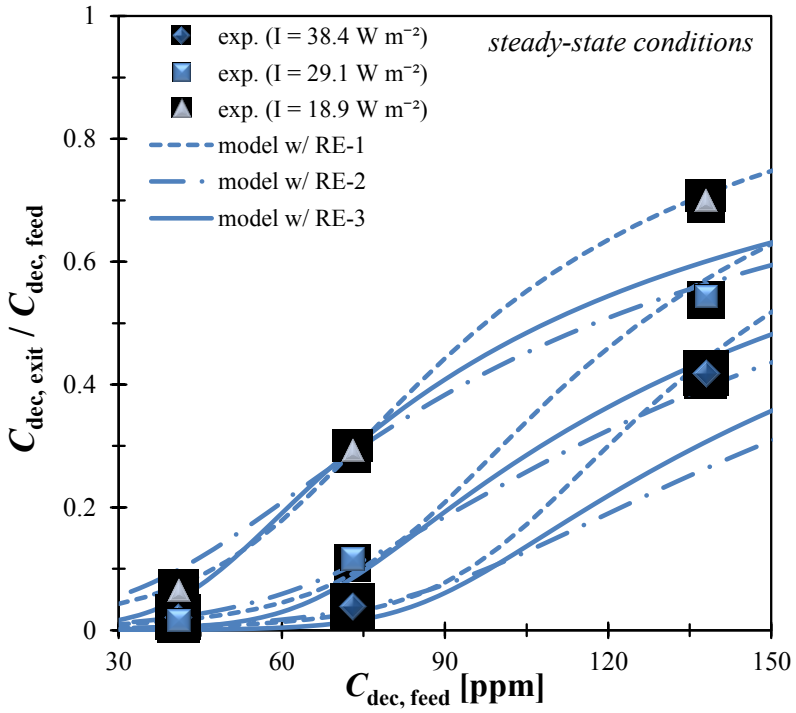

Fig. 5. Influence of the inlet concentration ($C_{dec, feed}$) on *n*-decane photodegradation fraction ($C_{dec, exit}$ / $C_{dec, feed}$, at steady-state conditions): experimental points for incident irradiance measured within 280-400 nm (sunlight UV fraction) of 38.4 W·m^{-2} (◆), 29.1 W·m^{-2} (■), and 18.9 W·m^{-2} (▲), and RE-1 (- - -), RE-2 (— · —), and RE-3 (——); Q_{feed}^{*} = 150 cm^3·min^{-1}, RH_{feed}^{a} = 40%, and T = 298 K; operation conditions reported in Table 2; * measured at 298 K and 1 bar.

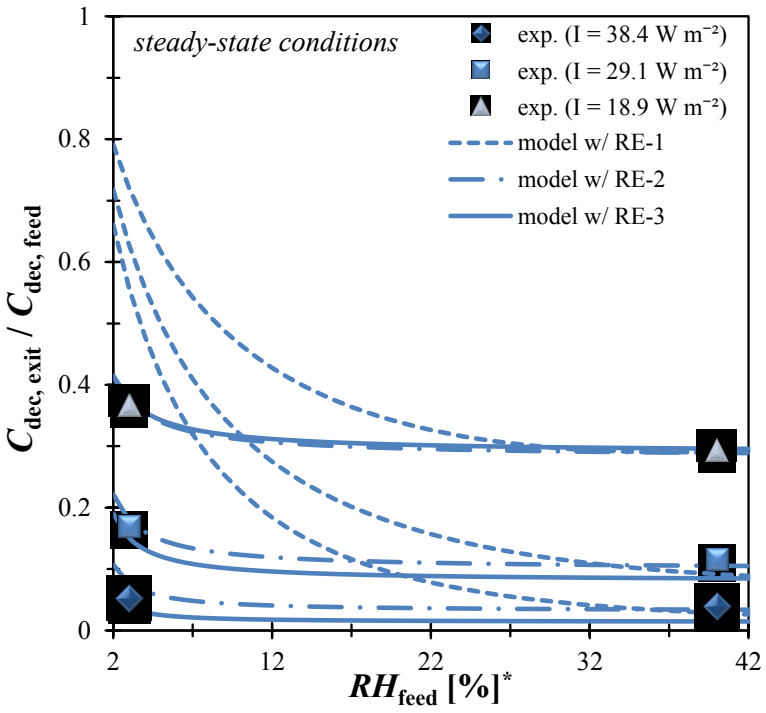

Fig. 6. Influence of the feed relative humidity (RH_{feed}) on *n*-decane photodegradation fraction ($C_{dec, exit}$ / $C_{dec, feed}$, at steady-state conditions): experimental points for incident irradiance measured within 280-400 nm (sunlight UV fraction) of 38.4 W·m^{-2} (◆), 29.1 W·m^{-2} (■), and 18.9 W·m^{-2} (▲), and RE-1 (- - -), RE-2 (— · —), and RE-3 (——); Q_{feed}^{*} = 150 cm^3·min^{-1}, $C_{dec, feed}$ = 73 ppm, and T = 298 K; operation conditions reported in Table 2; * measured at 298 K and 1 bar.

744

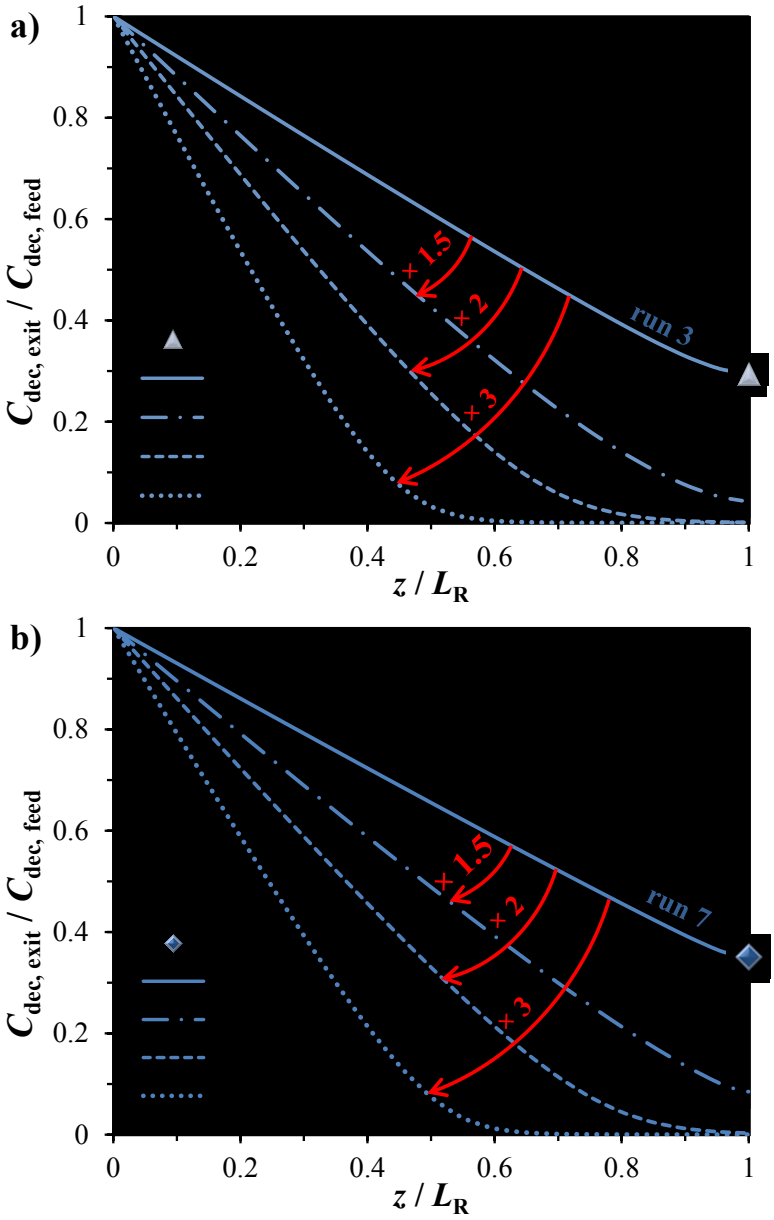

745

746 **Fig. 7.** *n*-Decane photodegradation fraction profiles ($C_{dec,\,exit}/C_{dec,\,feed}$, at steady-state
747 conditions) for photoreactors with different lengths [L_R]: 0.16 (—), 0.24 (– – –), 0.32 (- -
748 -), and 0.48 m (· · ·); (a) $C_{dec,\,feed}$ = 73 ppm, Q_{feed}^* = 150 mL min^{-1}, and I = 18.9 W m^{-2}
749 (measured within 280-400 nm: sunlight UV fraction); (b) $C_{dec,\,feed}$ = 73 ppm,
750 Q_{feed}^* = 300 mL min^{-1}, and I = 38.4 W m^{-2} (measured within 280–400 nm: sunlight UV
751 fraction); RH_{feed}^* = 30%, and T = 298 K; operation conditions reported in Table 2 (runs 3
752 and 7, respectively) (* measured at 298 K and 1 bar); experimental data (points);
753 mathematical modelling with RE-3 (lines).

754

755

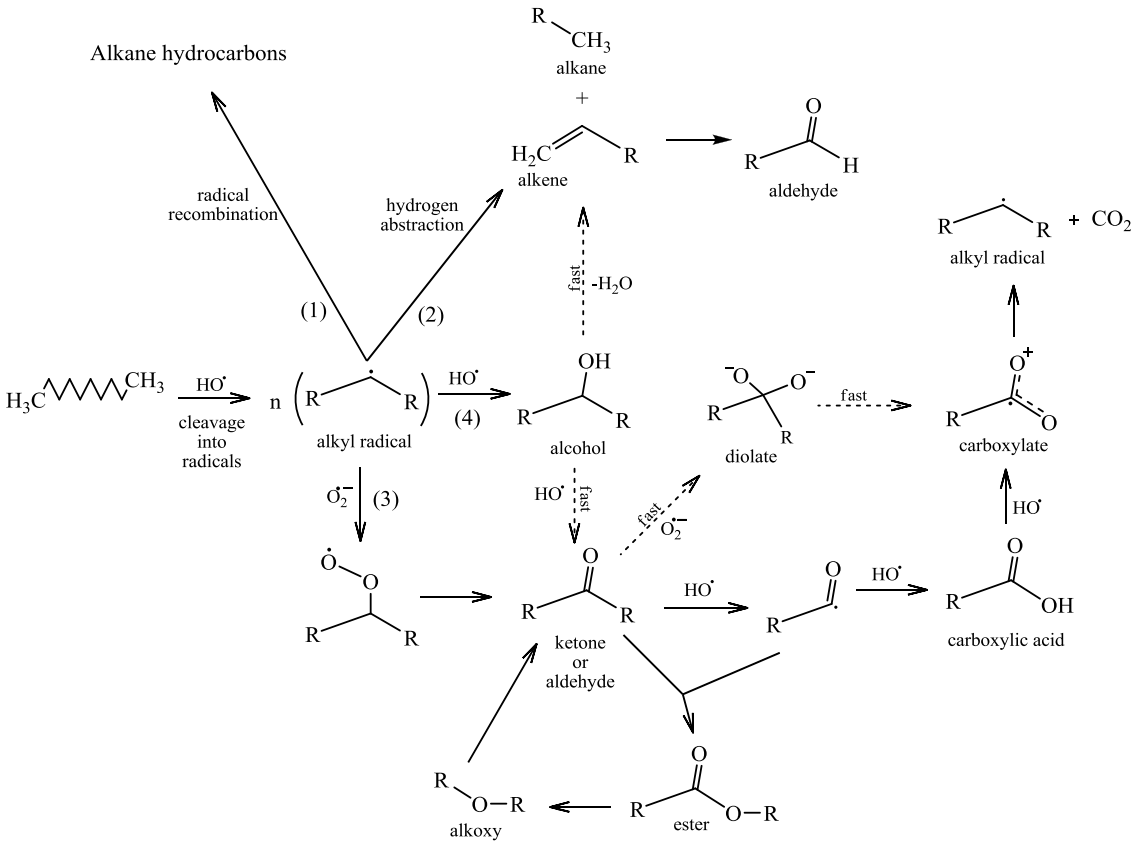

756

757 **Scheme 1.** Schematic representation of the reaction pathways proposed for the gas-phase

758 degradation of *n*-decane under simulated solar irradiation (R: alkyl roots or hydrogen).